Eigenmodes and symmetry selection mechanisms in circular large-aperture vertical-cavity surface-emitting lasers

I. V. Babushkin and N. A. Loiko*

Institute of Physics, Academy of Sciences of Belarus, Scaryna Prospekt 70, 220072 Minsk, Belarus

T. Ackemann

Institute for Applied Physics, University of Münster, Corrensstrasse 2-4, 48149 Münster, Germany

The characteristics of the spatial eigenmodes of vertical-cavity surface-emitting lasers with a large circular aperture are considered close to the lasing threshold. Experiments yield patterns based on rotational symmetry ("flowerlike" patterns) or on Cartesian symmetry (stripelike patterns) for very close operating conditions. The former are compatible with the boundary conditions whereas the latter are expected in infinite devices. Theoretically, the problem is considered in the framework of an eigenmode analysis of a linear partial differential equation for the optical field valid at threshold. This formulation allows for a simple implementation of asymmetries due to the reflection properties of Bragg mirrors as well as of transverse variations of gain and refractive index due to the device structure or due to imperfections in the growth process. A sharp transition between flowerlike modes and stripelike modes is shown to occur, if the device aperture is increased.

PACS number(s): 05.45.−a, 42.65.Sf, 42.60.Jf

I. INTRODUCTION

The spatial mode structure of vertical-cavity surface-emitting semiconductor lasers (VCSELs) has been a subject of considerable research during the last years (see, e.g., Refs. [1–11].

To a great extent, this is due to the fact that the spatial structure determines the spatial coherence and thus the brilliance of a laser beam, which is important, if large-aperture VCSELs are considered for high power application as free space communication, laser pumping or medical applications [4,12,13]. However, VCSELs are also investigated due to a general interest in spatial self-organization phenomena and pattern formation [5–7,9].

In *square* VCSELs stripelike modes were observed [5,14] which resembled very closely transverse Fourier modes (plane waves propagating off-axis of the resonator) and not Hermite-Gaussian (or LP) modes of high order. Emission of a single traveling plane wave is predicted for generic laser models [15,16] and the counter-propagating wave resulting in the observed stripe pattern can be generated due to boundary conditions in a laser with finite extent (e.g., Ref. [17]). Hence, the observed nonlinear pattern is also a mode of the linear laser structure. Beautiful example of more complex patterns arising due to interference of tilted waves reflected at the boundary conditions in square lasers were demonstrated in [9,18,19].

In lasers with a *circular* aperture [7], the boundaries are obviously not compatible with emission of an ideal transverse Fourier mode. Correspondingly, emission was found to be dominated by modes with a high order of (discrete) rotational symmetry being similar to Laguerre-Gaussian modes of high azimuthal order, nevertheless, also modes based on a

Cartesian symmetry and even stripelike modes were obtained, indicating that the selection between the different types is only "weak" (we use the term "Cartesian symmetry" to characterize stripelike modes as well as Hermite-Gaussian modes, see Sec. III for a more detailed discussion). In this paper, we are going to address the spatial mode structure of broad-area VCSELs in more detail. After a presentation of some experimental results, the question of pattern and symmetry selection at the laser threshold is addressed by an eigenmode analysis of a linearized partial differential equation for the optical field valid at threshold.

Our theoretical approach differs in some respect from the one conventionally taken in the determination of the threshold mode. Typically, analysis starts with a calculation of the eigenmodes of the "empty" cavity, i.e., the properties of the gain medium are not considered at this stage, though the calculation of the electromagnetic properties can be quite complete and rigorous reaching the level of fully vectorial calculations Refs. [8,20–22]. Then the modal gain is obtained by calculating overlap integrals of (material) gain and mode profiles (see, e.g. Refs. [8,23] for device structures similar to the one analyzed by us). Note that the material gain has a spectral dependence which might be important. This finally enables one to determine the mode selected at threshold.

In contrast, we obtain the modes of the field generated at threshold by considering a linearized equation for the laser field at threshold under certain lateral-boundary conditions. The eigensolutions of the such problem with highest growth rate give the spatial distribution of field at threshold, automatically taking into account both the symmetry of resonator and the properties of the active medium, included in the "underlying" system from which the linearized problem was obtained. This equation derived in Refs. [11,24–26] includes a general mechanism of pattern selection in lasers, based on a detuning of cavity resonance from a gain maximum

---

*Email address: nloiko@dragon.bas-net.by

[15,16,27], as well as a mechanism based on the spatial anisotropy created by Bragg reflectors. The problem is nonlocal, in general, mainly due to the influence of the Bragg reflectors. For the case of infinite homogeneous device it was solved using the transverse Fourier transformation [11,24–26], and it was shown, that due to this anisotropy, only two spatial Fourier modes have the lowest threshold instead of the whole continuum of modes with the same transverse wave number as in the isotropic problem. Therefore, for the anisotropic case, it is possible to gain some information on regular pattern formation already in the *linear* approximation, whereas in the isotropic case the nonlinear competition is strictly important for a further selection of modes.

Here, we study the problem for a transversely bounded device. To formulate a well defined mathematical problem, we approximate the nonlocalities by local terms (differential operators) using a technics similar to one developed in Ref. [28]. After this approximation we obtain an eigenproblem for a partial differential operator of the fourth order, which under suitable boundary conditions possesses a discrete spectrum. The eigenfunction with largest real part of eigenvalue gives the field distribution near threshold.

This formulation allows also for a simple implementation of transverse variations of the current (gain) or/and refractive index profiles. These inhomogeneities might be intended (e.g., the oxide aperture present in modern VCSEL device), due to parasitic effects (e.g., thermal lensing) or due to imperfections in the growth process. Hence, we are able to investigate how the spatial modes are affected by the boundary conditions and inhomogeneities inevitably present in any real semiconductor device.

We show that the symmetry properties of the field distribution at threshold depend very sensitively on the inhomogeneities and the diameter of the laser, and the transition between different types of symmetries can be very sharp.

The paper is organized as follows: Sec. II gives the experimental motivation of the work, clearly showing that circular large-aperture VCSEL can generate both flowerlike and Cartesian modes. Our theoretical approach is explained further in Sec. III, where the eigenproblem is first formulated and comparison with traditional rotationally symmetric systems is provided. In Sec. IV, the symmetry transitions with changing laser diameter are investigated in detail. In Sec. V the influence of inhomogeneities on the field distribution is examined. Section VI contains a summary and discussion of the results. The derivation of the linearized equation, as well as its approximation to obtain a local one, and methods of numerical solution of corresponding eigenproblem are addressed in Appendixes.

II. EXPERIMENT

In the following, we will describe some experimental results on spatial structures observed in broad-area bottom-emitting VCSELs. The aim of this section is to provide a motivation for the theoretical studies on symmetry properties, not a detailed study of device characteristics. Several aspects of devices of the type used were investigated before
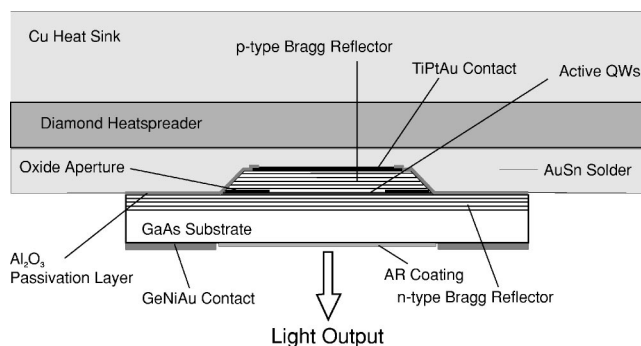

FIG. 1. Bottom emitting VCSEL soldered junction down on a diamond heat sink.

in Refs. [4,7,12,13]. We refer to these papers for details.

The devices under study are based on InGaAs/GaAs quantum wells embedded in a spacer layer with a thickness of one wavelength (Fig. 1). The emission wavelength is in the 950 nm spectral region. The cavity is closed by Bragg reflectors (*p* side: 30 stacks, reflectivity of nominally $R_1 > 0.9998$; *n* side: 20.5 stacks, $R_2 > 0.992$). The *p* side is textured by etching mesas down till the spacer layer which carry the *p*-contact pads. The size of the active area is defined by a 30 nm-thick oxide aperture which provides the current as well as the optical confinement. Emission takes place through the thinned, nearly transparent substrate. This *bottom-emitting* geometry provides a better uniformity of the current and carrier distribution in the active layer than a top-emitting one (i.e., where the emission is coupled out through the *p* mirror) since in this case the *p*-contact pad has to be ring shaped [29]. This was checked in our devices by taking images of the near field spontaneous emission profile well below threshold which should indicate the spatial carrier distribution. The observed irradiance is homogeneous to within 10–20 % but still has the maximum at the perimeter of the laser (and a local minimum at the center) due to residual current crowding at the oxide aperture. This is in agreement with the calculations presented in Ref. [29].

The metallized *n* side of the wafer is attached to a thin copper submount with a central bore for the emission. The *p* side is contacted with the help of a probe tip. Perturbations induced by the probe tip can be kept very small, if the contact is done at the perimeter of the contact pad. This is due to the fact that the diameter of the contact pad is slightly larger than the one of the active zone (e.g., 80μm compared to 54μm) and therefore a direct stress can be avoided. The wafer investigated has very similar nominal characteristics as the wafer considered in Ref. [7]. In one case, we present results from a device with a diameter of 38 μm, whose *p* contact is soldered on a diamond heatspreader (Fig. 1, Ref. [4]).

The experimental setup is rather simple. The copper submount with the VCSEL is attached to a thermoelectric cooling (Peltier) element for temperature control and stabilization. The output light is collected with an aspheric lens and focused on a charge-coupled device (CCD) camera such that the contrast of the boundary of the active area is optimized for the spontaneous emission below threshold. This corresponds to a near field imaging of the time-averaged intrac-
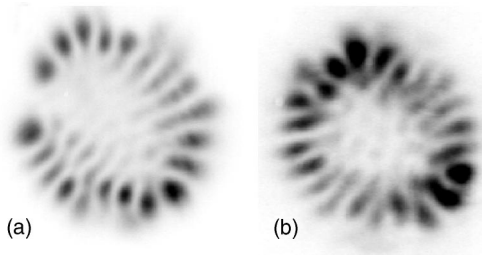
FIG. 2. Typical pattern obtained in the dominant polarization component at 10% above threshold in a device with a diameter of 54 μm. (a) Near field, (b) far field.

avity field intensity. Alternatively, the back focal plane of the collimator can be imaged on the CCD camera providing access to the far field intensity distribution of the emitted light. A combination of a Fresnel rhomb and a Glan-Thompson linear polarizer serves for polarization resolved detection.

Figure 2 shows a typical pattern observed close to threshold in devices with a diameter of 54 μm. It is a flowerlike pattern [Fig. 2(a)], i.e., it is characterized by a nearly circular arrangement of bright peaks at the perimeter of the laser. In the example presented here, the line of peaks has a defect in the upper left part of the laser. Similar defects are not untypical, but circular flowers exist also (see also the images in Ref. [7]). The average pitch along the perimeter is on the order of some micrometer (here 7 μm). Near [Fig. 2(a)] and far field [Fig. 2(b)] are rather similar but not exactly identical. This indicates that the structure is close to but not identical to a Laguerre-Gaussian mode.

These patterns should be considered as typical representatives of flowerlike patterns (see also Figs. 3 and 8 of Ref. [7]). They are obviously related to the principal circular symmetry of the laser which might be perturbed by some inhomogeneities.

Figure 3 shows a pattern obtained in a laser from the same array, i.e., from a laser, which should have very similar properties as the laser discussed before. Nevertheless, the observed pattern is quite different. In the near field it consists of a sequence of stripes which do not fill the aperture [Fig. 3(a)]. The far field is dominated very much by two peaks [Fig. 3(b)] indicating that the pattern is better characterized as stripes, i.e., as a transverse Fourier mode, than as a Hermite-Gaussian mode.

This issue is investigated further in Figs. 3(c) and 3(d). The amplitude of the lines is not uniform across the device—as it should be for perfect stripe patterns—but peaks at the sides. The amplitudes between center and perimeter have a ratio of about 0.5:1. However, in the far field pattern, the amplitude ratio is about 1:10, i.e., it is much lower than in the near field. Thus the observed structure is clearly not a Hermite-Gaussian mode, since Gaussian modes are self-similar on propagation. Thus we conclude that the boundary conditions do not permit the emergence of ideal stripes but that the observed patterns is a realization which is compatible with boundary conditions and possibly inhomogeneities. Similar structures were reported for other wafers in Ref. [7]. Apart from these stripelike structures and the flowerlike ones, patterns with a Cartesian symmetry are observed of
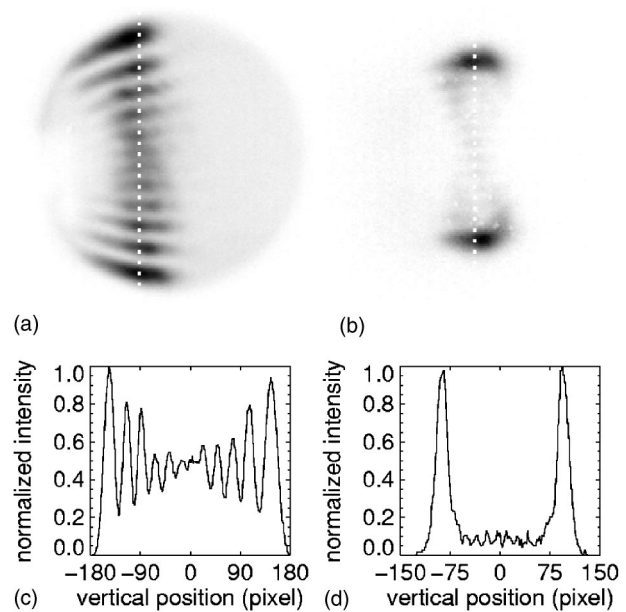

FIG. 3. Threshold pattern in the dominant polarization component in a device with a diameter of 54 μm (images shown obtained at 10% above threshold). (a) Near field, (b) far field, (c) cut through near field intensity distribution along line indicated, (d) cut through far field intensity distribution along line indicated.

which near and far field are rather similar (Fig. 4 of Ref. [7]).

The data show that in the wafer under study apparently the selection between modes with dominant rotational and Cartesian symmetry is weak, i.e., apparently small disturbances decide over the symmetry. This is further exemplified by the fact that sometimes the symmetry of the pattern changes in the course of time at nominally constant operating conditions. This happens probably in situations in which the strain on the device due to the contact tip is not negligible and some mechanical relaxation occurs which changes the stress condition. Such an observation also indicates that slight disturbances can mediate the transition from one situation to the other.

Figure 4 shows a situation, in which the near pattern field pattern at threshold does not fill the aperture [Fig. 4(a)]. The structures shows modulation across both axis and is rather irregular. The far field is dominated by off-axis contributions [Fig. 4(b)]. These observations indicate the existence of a gradient inhomogeneity in the device which might be either a gradient in cavity resonance or in pump current.

Interestingly, this inhomogeneity becomes smaller, if the current is increased [Fig. 4(c)] and essentially disappears for even high currents [Fig. 4(e)]. At the same time, the spectrum broadens to the high-frequency side reaching a width of about a THz (about 3.2 nm) for the conditions of Figs. 4(e) and 4(f). This indicates that the high-order transverse mode which are increasingly detuned from the longitudinal resonance have a higher rotational symmetry than the ones with a low detuning. This hints to the fact that the observed gradient inhomogeneity is due to a gradient in cavity length. Its existence is well known (e.g., Ref. [7]), if not the best portion around the center of the wafer are considered.
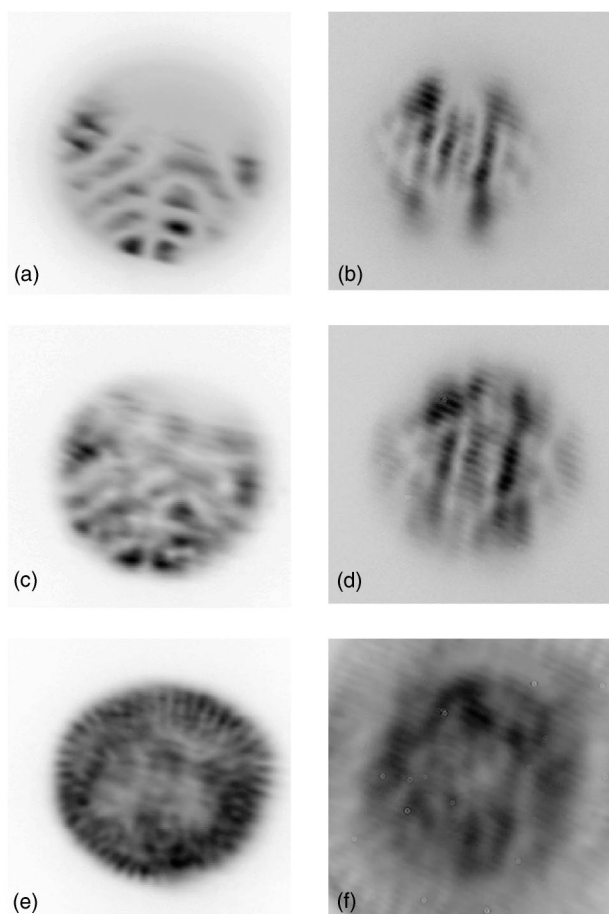
FIG. 4. Patterns obtained in the dominant polarization component in a device with a diameter of 38 μm mounted on a heat sink. (a),(c),(e) Near field and (b),(d),(f) far field. Distance above threshold: (a),(b) 6% (however the pattern is identical to the one obtained at 3% above threshold except for the fact that the contrast of the latter is lower); (c),(d) 56%; (e),(f) 938%.

III. THE EIGENPROBLEM AND MODE SELECTION

Motivated by the experimental observations, we are going to consider below the mode structure of broad-area VCSELs and the symmetry selection theoretically. We assume that the laser has a well defined linear polarization, that allows one to simplify the system description. That assumption stems from the fact that small (to a great extent uncontrolled) anisotropies select usually a well defined polarization state at threshold (e.g., Refs. [30–32], and references therein). Moreover, the patterns obtained in the two polarization components are similar as a rule that implies common mechanisms of their formation, so the extension to a vectorial model is rather straightforward.

As is known, there are two distinct types of descriptions for a laser operating near the lasing threshold. In the first one which is mostly used for small-aperture devices, the field $e(x,y)$ is decomposed into transverse eigenfunctions of the empty cavity [8,23,33]. Then, the modal gain needs to be computed by an overlap integral of the gain and the modal profile taking into account the frequency dependence of the material gain. After this procedure, it is possible to determine the mode with the lowest threshold. However, the shape of this mode takes into account only the properties of the empty cavity (boundary conditions and possible inhomogeneities).

The alternative approach was developed for a homogeneous laser with a large aperture in the limit of an infinitely extended system [15,27]. In that case the eigenmodes and their growth rates can be directly obtained from a linear stability analysis of the nonlasing zero solution of the nonlinear partial differential equations (PDEs) governing laser dynamics. The resulting eigenmodes are plane tilted waves (transverse Fourier modes) with definite wave vectors and their growth rates depend on the detuning of the longitudinal cavity resonance from the gain maximum [15]. For a laser with losses independent from wave vector orientation, those plane waves are selected by the critical value of wave number, i.e., by the modulus of transverse wave vector, and therefore the situation is highly degenerate. The pattern selection can be obtained only by taking nonlinear interactions into account (see, e.g., Refs. [27,34]).

As it was shown in Refs. [10,11,25] and confirmed by a more rigorous model [35], the rotational symmetry is broken for off-axis emission with a defined polarization even in the infinitely extended laser. This is due to the fact that the reflection coefficient of the Bragg reflectors enclosing the cavity depends on the angle between polarization vector and wave vector. For linear polarized wave there are two opposite directions of transverse wave vectors, with maximal reflection [56]. As a result, only two tilted waves (being the complex conjugates from each other) have minimal losses and become critical at the first laser threshold. In other words, there is a selection not only of the critical wave number but also the wave orientation due to the linear mechanism in comparison with the mentioned above case of a laser with isotropic cavity. The nonlinear competition takes place only between two selected traveling waves and standing wave created by them. This problem was discussed in Ref. [26].

In the case of square devices [5,35], those transverse Fourier modes are compatible with the lateral boundary conditions, and hence can be selected at threshold when the transverse area is finite. It is well known, that Gauss-Hermite modes (e.g., Ref. [36], for curved mirror resonators or wave guides with a parabolic refractive index profile) or Fourier modes (for homogeneous apertures) are the appropriate choice of eigenfunctions. In the latter case, the simplest possibility is a stripe pattern aligned to one of the sides. We will refer to these modes as "stemming from Cartesian symmetry" or shortly as "modes with Cartesian symmetry," since they have typically only a low-order rotational symmetry.

For circularly shaped devices with conventional isotropic mirrors, the situation is more complicated. The eigenmodes of the empty cavity satisfying the lateral ring boundary conditions are Gauss-Laguerre modes (in devices with a parabolic refractive index profile), the so-called LP-modes (linearly polarized modes based on Bessel functions) in devices with (weak) step-index wave guides (e.g., Ref. [37]) or Bessel modes in devices with a homogeneous refractive index profile. As in the infinite device these modes are highly degenerate in the case of rotationally symmetric systems, since the modes, obtained by a rotation by any angle, have the same growth rate at threshold.

We show below that if we account for the anisotropy induced by the Bragg reflectors (and possibly other imperfectness of the cavity), the mode appearing at threshold cannot be a pure rotationally symmetric or a pure stripelike modes, but something intermediate. In such an anisotropic situation only a few modes have the same threshold, and the pattern selection problem can be considered already on the stage of a linear approximation. Therefore we investigate an equation of the type

$$\frac{\partial e(x,y,t)}{\partial t} = \hat{O}_{(x,y)} e(x,y,t), \tag{1}$$

where $\hat{O}_{(x,y)}$ is a linear operator, acting in (x,y) space on the transverse profile $e(x,y,t)$ of the optical field at the laser threshold. From Eq. (1), the following eigenproblem is obtained:

$$\hat{O}_{(x,y)} e_g(x,y) - \lambda_g e_g(x,y) = 0. \tag{2}$$

Here, $\{g\}$ parametrizes the set of eigenmodes $e_g(x,y)$ with eigenvalues λ_g which are the spatial field distributions growing as a whole with rate $\mathrm{Re}\lambda_g$.

For a homogeneous device of an infinite aperture, the spectrum λ_g of Eq. (2) is continuous with eigenfunctions being transverse Fourier harmonics $e_g = \exp(i\mathbf{k}\mathbf{r})$ [where $\mathbf{k} = (k_x, k_y)$ and $\mathbf{r} = (x,y)$]. Their selection described above is determined by a maximal value of $\mathrm{Re}\lambda_g$ defined from the following dispersion relation:

$$O(k_x, k_y) = \lambda_g, \tag{3}$$

where $O(k_x, k_y)$ is defined through a transverse Fourier transform $\mathcal{F}$ of the field $e_g(x,y)$

$$\mathcal{F}: e_g(x,y) \mapsto e_g(k_x, k_y) = \int e_g(x,y) e^{-i(k_x x + k_y y)} dx dy, \tag{4}$$

as a multiplication in the transverse Fourier space:

$$\mathcal{F}[\hat{O}_{(x,y)} e_g(x,y)] \mapsto O(k_x, k_y) e_g(k_x, k_y). \tag{5}$$

The eigenproblem (2) with proper boundary conditions has a discrete spectrum, and it is evident from the physical nature of the problem that $\mathrm{Re}\lambda_g$ is bounded from above. In the following, we suppose that all λ_g are arranged in the order of decreasing of their real values: $\mathrm{Re}\lambda_1 \geq \mathrm{Re}\lambda_2 \geq \mathrm{Re}\lambda_3 \ldots$.

Such an approach includes both the frameworks mentioned: on one hand, the eigenproblem with certain lateral-boundary conditions accounts for the peculiarities of the empty cavity (such as the transverse shape of the device and inhomogeneities of the transverse area of the cavity [38,39]); on the other hand, this equation is the linearization of equations describing the laser at threshold that allows to take into account wavelength selection mechanism due to an interaction of light with active medium [34] and pump spatial profile. We restrict ourselves only to this linearized problem, leaving more complex effects as the influence of spatial hole burning [26,33,38,40] and the nonlinear competition of eigenmodes with nearly the same growth rate for further more detailed investigations.

Derivation of the Eq. (1) with operator $\hat{O}_{(x,y)}$ from basic laser equations is presented in Appendix A. In general, it is a pseudodifferential operator [41] including nonlocal integral terms. They arise because a part of the operator describing the light interaction with Bragg reflectors of the laser cavity is defined through the action in transverse Fourier space (4). However, it is possible to approximate this operator by a partial differential operator of the type

$$\hat{O}_{(x,y)} = \sum_{i,j=0}^{4} (-i)^{i+j} a_{ij} \frac{\partial^{i+j}}{\partial x^i y^j}. \tag{6}$$

The fact that the equation is of fourth order (instead of second) ensures the existence of a maximum of the dispersion curve (3) for nonzero $\mathbf{k}$ at suitable parameters as for an infinite homogeneous device. The derivation of such an approximation is described in Appendix B.

The coefficients a_{ij} are complex-valued in general. The imaginary part of coefficients appears from two different sources. The first one is the usual diffraction term of the form $ia\Delta$ (where Δ is transverse Lapalcian, and a is a diffraction coefficient). It gives a contribution only to coefficients a_{02} and a_{20}. The second part giving contribution into all a_{ij} is a result of the field phase shift at reflection from the complex distributed Bragg structure.

The simplest way to model of the finiteness of a real device is imposing of zero boundary condition for $e_g(x,y)$ at the end of aperture. For a circular aperture it takes the following form:

$$e_g(x,y)|_{|\mathbf{r}|^2 = R^2} = 0. \tag{7}$$

This condition is confirmed by the fact that both gain and field intensity decrease rapidly close to the aperture. In fact, this condition is not sufficient for a solution of Eq. (6), because this equation is of fourth order. One should provide a second boundary condition including the derivatives of the field which has to satisfy so called Lopatinsky (or ellipticity) condition [41]. It is clear that the second condition also should be consistent with the decreasing of the field far away from the aperture Therefore some combination of spatial derivatives of the field should be zero. From the reflection symmetry of the operator $\hat{O}_{(x,y)}$, it follows that this combination can contain only derivatives of even order. In general, the second boundary condition must be

$$\hat{T} e_g(x,y)|_{|\mathbf{r}|^2 = R^2} = 0, \tag{8}$$

where $\hat{T}$ is

$$\hat{T} = t \frac{\partial^2}{\partial x^2} + \frac{\partial^2}{\partial y^2}. \tag{9}$$

with complex coefficient t. We do not assume in this paper any anisotropy introduced by boundary conditions, hence we should take $t = 1$. Then the second condition becomes the same as for an isotropic device which arises automatically in the last case due to reducing the operator (6) to the next one:

$$\hat{O}_{(x,y)} = b_1\Delta^2 + b_2\Delta + b_3, \tag{10}$$

[b_1, b_2, b_3 are some (in general complex) coefficients], and due to the equality (7). One can easily recognize in Eq. (10) the linear part of the well known Swift-Hohenberg equation [16,27], describing the evolution of a laser field near threshold. Therefore, the anisotropic operator (6) corresponds to a generalization of the spatial parts of the Swift-Hohenberg-like order parameter equations [16,34] obtained from the usual "uniform-field"-models often used to model pattern formation problems in cavities [15,16,34,42], since it allows for an asymmetry in k space.

To the best of our knowledge, there is no analytical solution of the general eigenproblem (2) with the operator (6). However, the problem can be solved numerically by reducing this equation to a system of two equations of second order (see Appendix C). For that, an auxiliary function is introduced and the simple numerical procedure can be used when the zero boundary condition as Eq. (7) is imposed on it. However, this corresponds to the use of second boundary condition (8) of the original problem with $t \neq 1$. The value of this parameter is determined by the inner anisotropy of the operator (6). It is comparatively small, and the obtained solution is very close to a solution of the problem with isotropic boundary condition (8) with $t=1$ (see Appendix C).

It will turn out, that the anisotropy of the problem and the circularly boundary conditions are competing in the determination of the eigenfunctions of (6). Hence, with decreasing diameter of the aperture the solutions of the problem undergoes a transition from a solution which is a superposition of two transverse Fourier modes (as for the infinite aperture case) to the flowerlike eigenfunctions of the isotropic operator (10). In the following section we consider this transition, taking as a starting point the problem (2) with the operator (6) and boundary conditions (7),(8).

Up to now, we assumed a homogeneous pump and refractive index profile. However, in real devices there are additional inhomogeneities of current density, resonator length or refractive index. To describe index inhomogeneities, given by $n_i(x,y)$, and to take into account possible inhomogeneity of the current density $\delta\mu$ the operator $\hat{O}_{(x,y)}$ should be considered in the following form:

$$\hat{O}_{(x,y)} = \sum_{i,j=0}^{4} (-i)^{i+j} a_{ij} \frac{\partial^{i+j}}{\partial x^i y^j} + i\, ln_i(x,y) + g_{00}\delta\mu(x,y), \tag{11}$$

where the derivation and the coefficients g_{00}, l are addressed in Appendix B. The influence of inhomogeneities in Eq. (11) on symmetry properties of the eigenmodes is considered in Sec. V.

IV. THE COMPETITION OF SYMMETRIES IN A HOMOGENOUS DEVICE

A. Simplified example: Eigenvalue problem with real coefficients

In order to explain the principles of reasoning and to investigate the general tendency in the transition between modes with dominant Cartesian and dominant rotational symmetry, we start from the simplified case of Eq. (6) and assume that the coefficients in Eq. (6) are real valued.

In that case the eigenvalues of Eq. (2) are known to be also real valued. Moreover, the transverse Fourier spectrum $e_g(k_x, k_y)$ of the eigenfunction corresponding to some eigenvalue λ_g is a generalized function (distribution) which is nonzero *only* on a curve $S_g(k_x, k_y)$, defined as a set of zeros of the polynomial (3) [41].

Therefore, the characteristics and the anisotropy of an eigenfunction is *completely* determined by the topological and symmetry characteristics of the curve (3) in (k_x, k_y) space for a defined value of λ_g. Obviously, it depends on the particular value of λ_g.

For example, in the isotropic case (10) with real coefficients b_i, the eigenfunctions are known to be also eigenfunctions of Helmholtz equation, being generalized function of the form

$$e_g(k_x, k_y) = \exp(in\phi_S)\delta_S, \tag{12}$$

where S is a circle of radius R_g which is connected to λ_g by the relation $\lambda_g = b_1 R_g^2 + b_2 R_g + b_3$, δ_S is a Dirac δ function which is zero everywhere except on S, and ϕ_S is an angular coordinate on S [43].

We can characterize the spatial anisotropy of Eq. (6) by comparing it with the nearest operator of type (10). The surface $O(k_x, k_y)$ for dispersion relation (3) (that corresponds to the surface of possible λ_g for an infinite case) is displayed in Fig. 5(a) for some model coefficients in Eq. (6). The example of its intersection by a plane corresponding to some eigenvalue λ_g for a finite case is also presented. As was mentioned above the transverse Fourier harmonics of the corresponding eigenfunction e_g are nonzero only on the curve S_g obtained from this intersection.

Figure 5(b) shows such curves S_g for the eigenfunctions in transverse Fourier space for values of λ_1 corresponding to the first unstable eigenfunctions of devices of different size (solid lines). The corresponding curves for the closest operator of type (10) are displayed as dashed lines. For an isotropic operator (10) λ_g can be found analytically for given radius of the aperture R. It can be easily shown [43] that $R_g = \mu_g/R$, where μ_g is gth zero of zero order Bessel function $J_0(\mu)$. Therefore, the outermost curve corresponds to a small device, the inner ones correspond to devices of larger aperture. It is worth noting that similar plots are obtained when a spectrum of eigenmodes for a single device is considered.

It is evident that the curves with a large diameter—i.e., the ones corresponding to small devices—are quite similar to circles. In this case, the anisotropy of Eq. (3) is not noticeable and the eigenfunctions can be described by distributions similar to Eq. (12), resembling flowerlike pattern. From the second point of view mentioned above, these curves present the spectrum of high-order eigenmodes—i.e., modes with smaller eigenvalues λ_g—for a single device with fixed diameter. This implies that the eigenfunctions of higher-order eigenmodes are less anisotropic.

If the diameter is increased, the topmost eigenvalue tends to the absolute maximum and reaches it in the limit of infi-
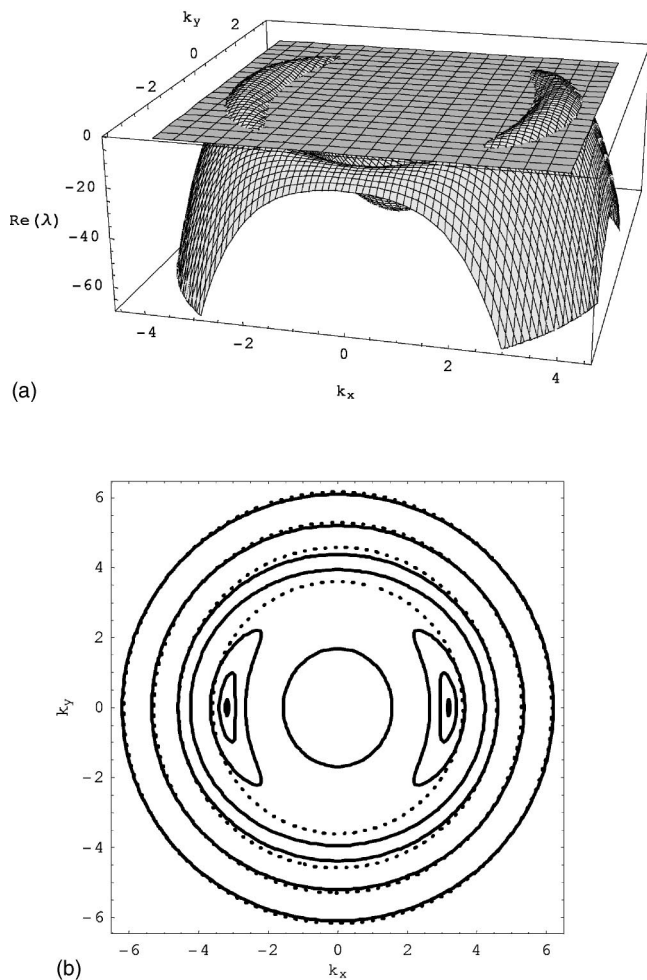
(a)

FIG. 5. Illustration of the qualitative behavior of eigenfunctions. (a) Surface of the real part of λ_g in dependency on (k_x, k_y) defined by Eq. (3) for model parameters $a_{00} = -52, a_{02} = 10.2, a_{20} = 9.18, a_{22} = -1, a_{04} = -0.5, a_{40} = -0.5$. (b) corresponding curves S of eigenfunctions for different values of λ_g (solid lines). They are obtained as cross sections of the surface in (a) with planes $\lambda_g = \text{const}$ [one of which is shown in (a)]. A decreasing sequence of λ_g can be obtained by either increasing the diameter and considering the largest eigenvalue λ_1 for each diameter, or by considering the sequence λ_g for $g = 1, 2, \ldots$ for a device with fixed diameter (in both cases the λ_g are assumed to be an ordered set $\lambda_1 \geq \lambda_2 \geq \ldots$, the first value giving the most unstable mode). The same curves are shown for the closest operator of type (10) for comparison (dotted line).

nite diameter, when the corresponding curve S shrinks to two points in transverse Fourier space, giving a stripelike pattern of the form $\exp(i\mathbf{k}_m\mathbf{r}) + \text{c.c}$ in (x, y) space [where $\pm\mathbf{k}_m$ are the coordinates of the maxima of the surface (3)]. From this note, one can easily find two manifestations of spatial anisotropy. The first one is obvious for very large diameters, when the line S breaks into two disconnected ones, each of them having the center at $\pm\mathbf{k}_m$. At that two transverse counter-running waves appear in the (x, y) space. The second manifestation stems from the fact that each connected part of the curve deviates from an ideal circle. Although an analysis is difficult in the general, for the simple case when the curve S can be transformed to a circle by a linear coordinate trans-
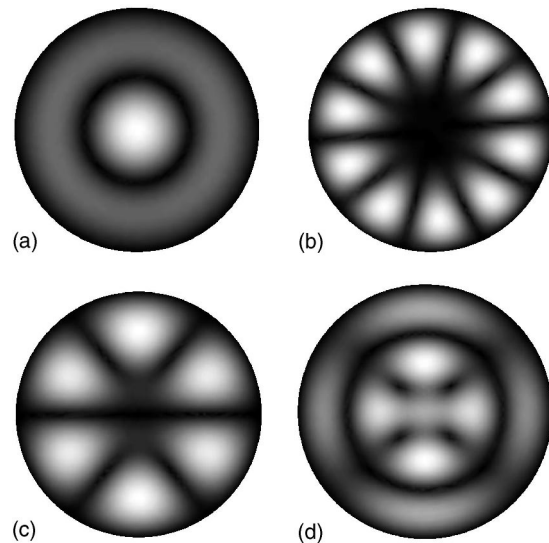

FIG. 6. The two first eigenmodes of the homogeneous operator (6) with boundary conditions (7),(8) for the case of rather small aperture and the detuning $\delta = 10$ nm. (a),(b) $2R = 12.5$ μm, difference in the threshold of the first and the second mode is 2.6%. (c),(d) $2R = 20$ μm, difference in the threshold is 0.5%.

formation (the boundary conditions in real space will then be zero on an ellipse instead of a circle), the solutions of the problem can be expressed in terms of Matheiu functions.

B. The laser case: Complex coefficients

For the laser equations, the coefficients a_{ij} are complex valued. In this case the eigenvalues are also complex and it is not possible anymore to represent the eigenfunctions as distributions on some curve, defined as a cross section of a surface at some plane [41,43]. Therefore, a simple representation like one in Fig. 5 is not possible. However, we show below that the qualitative behavior of the eigenfunctions will be the same as in the preceding case.

This statement is illustrated by Figs. 6 and 7. It is easy to see that for a small diameter the first mode is rather rotationally symmetric and is similar to a fundamental one for an empty cavity [Fig. 6(a)].

The second eigenmode [Fig. 6(b)] has zero intensity in the beam center and the emission is formed by an even number of "petals" arranged in a circular manner. It is nearly degenerate in growth rate with the first one. If the device diameter is increased, this mode becomes the first eigenmode and the number of petals increases [Fig. 6(c)]. The image illustrates that it is not necessary to invoke a current enhancement at the edges due to the peculiarities of the VCSEL design [7,39] in order to explain the appearance of such modes. Nevertheless, we will see in the following section that even a slight current crowding can shift the eigenvalue of a flowerlike pattern to the top even in the case when its growth rate in a homogeneous device is not the maximal one.

If the diameter is increased, the anisotropy of the operator coefficients becomes important, as shown in Fig. 5. Thus, the first mode is a stripelike pattern (Fig. 7). The pattern in the
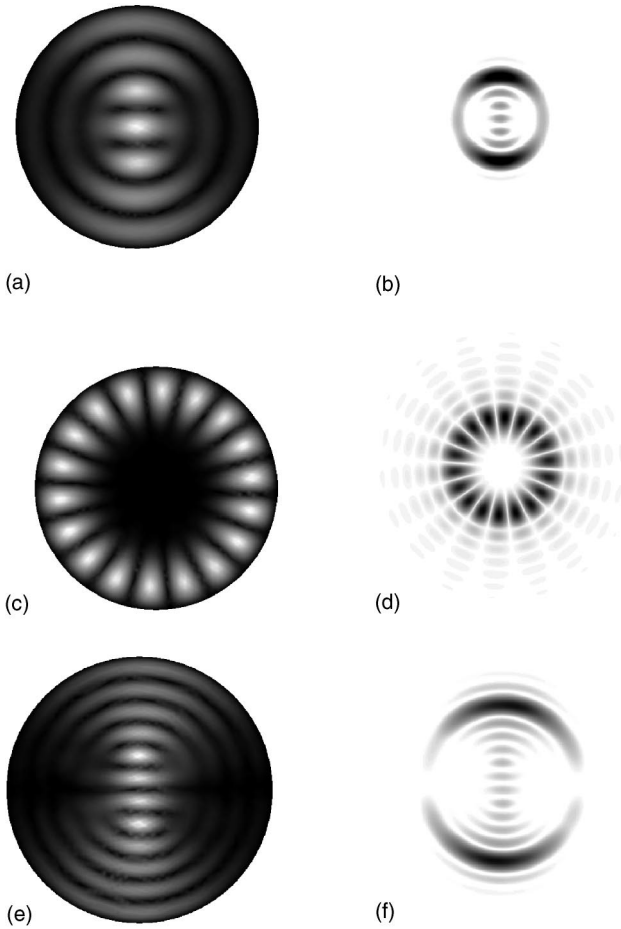
(a)

(b)

(c)

(d)

(e)

(f)

FIG. 7. The first (a),(b) and the second (c),(d) eigenmodes for the diameter $2R=36$ μm ($\delta=6.5$ nm, difference in the threshold of the modes is 0.09%). In (e),(f) the first eigenmode for $2R=55$ μm (and the same δ) is shown. The subsequent several modes for the case (e),(f) have the same symmetry. The first flowerlike eigenmode in this sequence is for $g=11$, and it resembles the one shown in Fig. 8. (a),(c),(e) are the near field intensity distribution, (b),(d),(f)—the far field intensity distribution.

Fig. 7(a) is not self-similar after a transverse Fourier transform [Fig. 7(b)], but has a rather pronounced Cartesian symmetry, especially far from the boundary. However, neighboring eigenmodes can have a completely different symmetry, as shown in Fig. 7(c). The second mode, having a very close threshold value, is a Laguere-like or Bessel-like function, with the same flowerlike picture in the far field.

With further increasing diameter, the difference in growth rate between neighboring modes tends to zero, and one can find more and more eigenmodes, falling in a fixed interval of growth rates above threshold. As in the case shown in Fig. 5, these modes keep the asymmetry of the operator (6), and the Cartesian symmetry of the first mode becomes more evident [Figs. 7(e) and 7(f)].

The number of stripes as well as number of spots in flowerlike pattern strictly depends on the coefficients of $\hat{O}_{(x,y)}$ which in turn depends on the parameters of the original system. The main length scale selection mechanism in a framework of the basic model is connected to the detuning. With

increasing the detuning, on the analogy of the infinite case [16,44] the spatial wave vector with maximal growth rate is increased, leading to increasing number of spots in the finite case, both for stripelike and flowerlike patterns. For the negative detuning, a pattern like in Fig. 6(a) appears first in the sequence of eigenfunctions.

V. THE INHOMOGENEOUS CASE

As it is shown in Appendix B, inhomogeneities of index and small inhomogeneities of current in the device can be modeled by simple additive terms, with the operator (11) instead of Eq. (6). The boundary conditions (7),(8) must be kept to provide a discrete set of eigenmodes.

The most noticeable type of pump inhomogeneities is pump crowding, appearing for large enough device aperture [7,29,39]. Due the construction of the device, the pump is more pronounced near the edges of aperture. In the numerical simulations, such type of inhomogeneity is modeled by the following function:

$$\delta\mu = \begin{cases} m \exp\left(-\dfrac{(|\mathbf{r}|-R_0)^2}{2\sigma^2}\right), & |\mathbf{r}| < R_0 \\ m, & |\mathbf{r}| > R_0, \end{cases} \quad (13)$$

where $r=\sqrt{x^2+y^2}$, m is the depth, R_0 is the width of the profile, and σ defines the half-width of the "transient area."

For a tiny inhomogeneity, the shape of eigenfunctions of operator (11) is almost not changed compared to Eq. (6), and the shift of eigenvalues is also very small. However, for large enough diameter, such as that presented in Figs. 7(e) and 7(f), eigenvalues are very close together, and even small inhomogeneity can change the order of eigenfunctions.

In this "perturbative" case, the shift in $\mathrm{Re}\lambda_g$ depends on the overlap integral of the inhomogeneity $\delta\mu(x,y)$ with the corresponding eigenfunction of Eq. (6) [45]. Figures 8(a) and 8(b) show the first eigenmode of operator (11) with tiny gain crowding for parameters as in Figs. 7(e) and 7(f). This mode would be the eigenmode of operator (6), with a threshold different only by 1.5% from the first mode, shown in Figs. 7(e) and 7(f). Thus, tiny inhomogeneity leads to preference of flowerlike pattern instead of stripelike. The stripelike pattern does not disappear, but it is shifted to the bottom in the set of eigenvalues.

Along with pumping inhomogeneities, there are several types of inhomogeneities of the refraction index. The most pronounced is the index gradient due to oxide aperture [38,46]. Numerically, it is realized by adding a term n_i proportional to Eq. (13) which is sharp enough ($\sigma=0.01R$), and R_0 close to R. In this case, the circular symmetry of inhomogeneity is strong enough to hide the anisotropy of the operator $O_{(x,y)}$, and the pictures are analogous to Figs. 8(a) and 8(b).

Another inhomogeneity is also often encountered in some devices: it is a constant gradient of the cavity length related to peculiarities of fabrication. This gradient, if not too strong, is equivalent to the gradient of index [47,48], because the additional phase shift introduced by such an inhomogeneity can be compensated by introducing a term of a type $in_i(x,y)$.
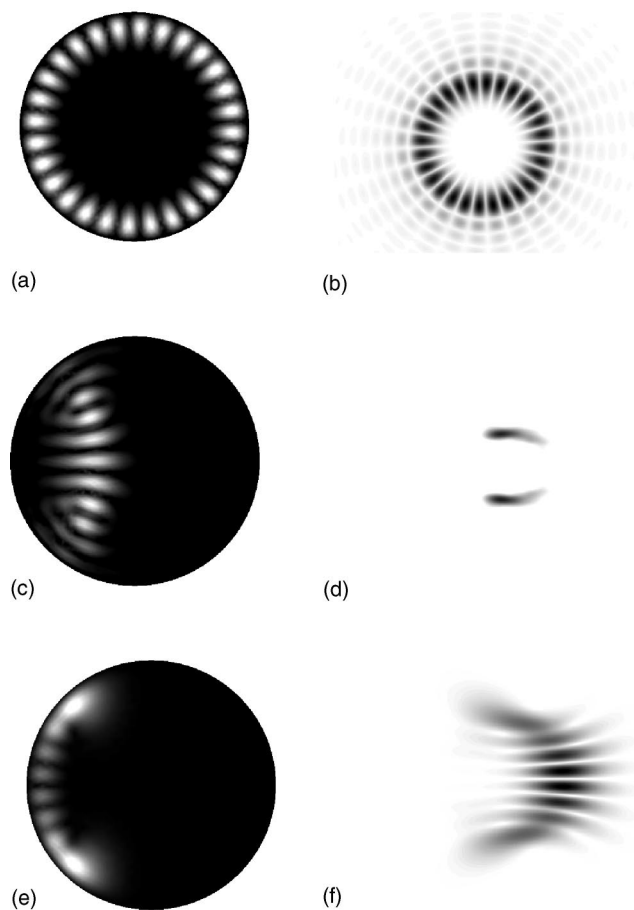
(a)

(b)

(c)

(d)

(e)

(f)

FIG. 8. (a),(b) first eigenmode for pump crowding, given by Eq. (13) with $\sigma=0.25R$, $m=6.0\times10^{-4}$, $R_0=0.95R$ and other parameters as in Figs. 7(e) and 7(f). (c),(d) the first and (e),(f) the second eigenmodes for pump crowding as in (a),(b), and index gradient $n_i=2.8\times10^{-4}x$. The second one has threshold 2% higher but becomes the first for $\sigma=0.1R$. (a),(c),(e) is the near field, (b),(d),(f) is the far field. The size of the device is as in Fig. 7.

(a)

(b)

(c)

FIG. 9. The first (a) and two subsequent, namely, 5th (b), and 10th (c) eigenmodes for $2R=36$ μm, and other parameters as in Figs. 8(c)–8(f). The eigenmodes with higher threshold fills the aperture better, in analogy with Fig. 4.

As above noted, small enough inhomogeneities leads to an exchanges of eigenfunctions without significant changes of their shape. The situation becomes different, if the amplitude of the inhomogeneities is increased. This is evident in Figs. 8(c)–8(f), where we model a linear index gradient, keeping at the same time gain crowding. It is clearly seen that the eigenfunction in the case of Figs. 8(c) and 8(d) preserves the shape of stripelike structures, and becomes even more Cartesianlike, than Figs. 7(d) and 7(e) (since the spots in far field are more pronounced). Again in this case, one can see a competition between the eigenmodes with completely different symmetry properties, as in the case of Figs. 7(a) and 7(c). But now these modes are Cartesianlike [Figs. 8(c) and 8(d)] and spotlike [Figs. 8(e) and 8(f)]. Very slight changes of σ in Eq. (13) leads to a change of the order of these modes.

One can see that low order eigenmodes for both homogeneous (Figs. 6 and 7) and inhomogeneous (Fig. 8) index and pump profiles demonstrate only partial filling of the aperture. However, the subsequent higher order modes often fill the aperture more homogeneously, even for inhomogeneous
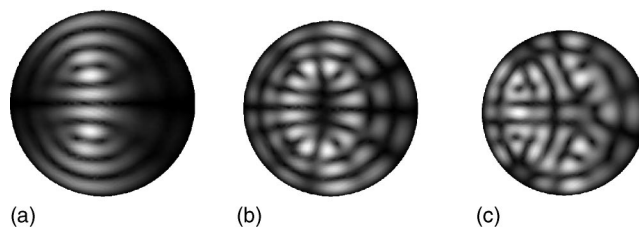
case. This is illustrated in Fig. 9, where the 1st, 5th, and 10th eigenmodes are presented. This figure provide the analogy with Fig. 4 which also shows a more homogeneous aperture filling with increasing current.

VI. DISCUSSION AND CONCLUSION

In this paper the competition of symmetry properties of patterns in VCSEL with wide circular aperture is considered. Experiments yield patterns based on rotational symmetry or on Cartesian symmetry for very close operating conditions. Two different kinds of symmetry are shown to be created by different sources: the rotational symmetry of the device aperture and the Bragg reflector anisotropy, selecting a certain direction in the transverse plane. The system was analyzed in the framework of linearized equations describing a VCSEL near threshold with lateral boundary conditions corresponding to the fast decay of the field towards the boundary. The linearization and approximation procedure (described in Appendixes A and B) gives an operator (11) acting in (x,y) space. The eigenfunctions and eigenvalues of this operator give the pattern with a maximal growth rate at threshold, appearing first after onset of generation.

The solution of the eigenproblem is a discrete set of functions, the separation between their eigenvalues is decreased with increasing device aperture. It is shown that for a small aperture the preferred type of pattern is a "fundamental" one, with a maximum in the center and nearly rotationally symmetric shape. For larger diameter, more complicated patterns appear at threshold. It is noticeable that flowerlike patterns which are located mainly near the boundaries often have the smallest threshold despite of there are no inhomogeneities in operator, making this kind of patterns preferable. With further increasing the diameter, the spatial anisotropy of the system becomes important, and smallest threshold has in this case stripelike pattern, aligned along the anisotropy direction.

However, eigenfunctions with completely different symmetries, namely with very high order of rotational symmetry, have eigenvalues (and therefore thresholds) very close to stripelike patterns, making the symmetry of pattern at the threshold very sensitive to small inhomogeneities both of the refraction index and pumping level across the cavity. Very small inhomogeneities only shift eigenvalues without changing of the shape of eigenfunctions, and this often leads to altering the order of patterns with different symmetry prop-

erties. In a first approximation, for such a tiny inhomogeneities the preferred pattern at threshold depends on the overlap integral of the corresponding eigenfunction with the inhomogeneity which leads to the preference of "rotationally symmetric" patterns (in the sense discussed in Sec. III) for the most often encountered circularly symmetric inhomogeneities. It should be noted, that very sharp transitions between different spatial patterns of the same symmetry due to strong sensitivity to small parameter variations was reported for optical parametric oscillator [51].

If the inhomogeneity is increased, eigenfunctions change significantly their shape. For example, for a gradient inhomogeneity of index along a fixed direction, patterns which only partially fill the aperture and concentrate around one side of it are preferable. Among them are deformed stripelike patterns [Figs. 8(c) and 8(d)] and spotlike patterns [Figs. 8(e) and 8(f)]. The subsequent eigenfunctions for that case fill the aperture more homogeneously (Fig. 9) which gives some explanation the increase of homogeneity of emission with increasing of pump level, observed experimentally (Fig. 2).

The form of the linear operator (11) is quite general and does not depend on the concrete model from which it was derived. As it is shown in the paper, if the operator is spatially anisotropic, it is enough to confine oneself by a linear approximation to describe qualitatively the competition of the symmetries of patterns. Moreover, as it was shown in Refs. [9,18], the patterns obtained in a VCSEL can be very complex, but can be explained, nevertheless, as eigenfunctions of Helmholtz equation of high order, or a combination a few of such functions. With the linear operator (6) or (11) derived in the present work, one can easily obtain the eigenfunctions which resembles eigenfunctions of high order of Hemholtz equation, but having the lowest threshold (largest real part of eigenvalue).

The main physical mechanism, defining the length scale of resulting patterns in the underlying model is the detuning of the cavity resonance from the gain maxima. Unfortunately, such a simple model is not able to explain the experimentally observed patterns at a negative detuning. However, some mechanisms which are not accounted for by the underlying model, can be simply introduced by just a shift of the detuning. One of them is local field correction [49,50] which effectively changes the detuning by quantity bd, where b is constant, proportional to the ratio λ/l of wavelength of the laser and the thickness of the active layer and can be therefore noticeable for VCSEL, where latter is small. Therefore, for numerical simulation in this paper the value of detuning was adjusted to give approximately the same number of stripes in the device aperture as in the experiments. It should also be noted that there are always at least two concurrent eigenfunctions with the same eigenvalue, with no competition in a linear approximation. To describe such a competition as well as an influence of transverse hole burning which is also become important already very close to threshold [26,27], nonlinear terms should be added. All this is being a subject of subsequent investigations.

APPENDIX A: THE BASIC EQUATIONS

The underlying model was introduced and considered in Refs. [10,11,25,26,48]. The system consists of evolution equations, describing the behavior of the slow field amplitude $e(t,x,y)$ and population inversion profile $d(t,x,y)$:

$$\dot{e} = -\hat{L}e + \hat{G}(de), \tag{A1}$$

$$\dot{d} = -d + \mu - \text{Im}[(i-\alpha)e^*\hat{\mathcal{L}}(de)], \tag{A2}$$

where κ is the field decay rate, and α is the linewidth enhancement factor [52]. As noted above we restrict the consideration to only one polarization component of field. In comparison with Refs. [10,11,25,26], we allow here for the dependence of the pump parameter μ and of the refraction index n on (x,y). The operators $\hat{L}=\kappa(\hat{F}_L/F_{L0}+i\alpha)+iln_i$ and $\hat{G}=\kappa(1+i\alpha)(\hat{F}_G/F_{G0})\hat{\mathcal{L}}$ describes loses and gain in the laser. The operators $\hat{F}_L=1-\hat{F}^2$ and $\hat{F}_G=(1+\hat{F})^2$ are related to the operator $\hat{F}$ of propagation of the light in one half part of the cavity (both parts assumed to be identical) calculated in paraxial approximation and including the anisotropic reflection from the Bragg reflector as well the propagation in the spacer layer. $\hat{F}$ is a function in (k_x,k_y) space [here, (k_x,k_y) are variables conjugated to (x,y) by the transverse Fourier transform (4), and $F_{G(L)0}=F_{[G(L)]}(k_x=k_y=0)$]. The term including n_i accounts for an inhomogeneity of the refraction index in index guided devices. It is introduced accordingly to well known effective index approach [47], when an index gradient is averaged over the cavity length, giving the same total phase shift as the initial one. The coefficient $l=\tau\omega/n_0$ is expressed via the optical frequency ω, time passage τ of light through the cavity, and the mean index n_0. The operator $\hat{\mathcal{L}}$ describes the gain contour shape. Here we take a simple Lorentzian profile of the gain line $\hat{\mathcal{L}}\xrightarrow{\mathcal{F}}\mathcal{L}(k_x,k_y)=1/(1+(\delta-\Omega(k_x,k_y))^2/\gamma^2)$, where $\delta=\omega_g-\omega_c$ is the detuning of the peak of the gain spectrum from the cavity resonance, γ determines the linewidth of the gain, and $\Omega(k_x,k_y)$ is a cavity frequency for every tilted wave (k_x,k_y).

To derive the linear evolution equation of the form (1), using the basic equations (A1) and (A2), we take into account that at the laser threshold two branches of the steady state solutions cross each other: the zero solution ($e=0$), and the nonzero lasing one. Because of the lasing solution at the cross-section point is characterized by $e=0$ and $d=\mu$ the further analysis is drastically simplified giving the following diagonal operator of the linearized problem:

$$\hat{\mathbf{O}} = \begin{pmatrix} \hat{O}_{11} & 0 \\ 0 & \hat{O}_{22} \end{pmatrix}. \tag{A3}$$

The diagonal form of Eq. (A3) shows, that the field e and the carrier density d are independent of each other at the laser threshold, and as it easy to see, the spectrum for $\hat{O}_{22}$ lies entirely in the half-plane $\mathrm{Re}\lambda \leqslant 0$, hence we can consider only the equation for the field (1) (with $\hat{O}_{(x,y)} \equiv \hat{O}_{11}$). $\hat{O}_{(x,y)}$ includes the current density at threshold $d = \mu$. From Eqs. (A1) and (A3) the explicit value for the operator $\hat{O}_{(x,y)}$ is defined by the following action on the field e:

$$\hat{O}_{(x,y)}e = -\hat{L}e + \hat{G}(\mu \times e). \tag{A4}$$

In the case, when there are no inhomogeneities of pump μ and index n_i, Eq. (A4) can be written in transverse Fourier space:

$$O(\mathbf{k}) = -L(\mathbf{k}) + \mu G(\mathbf{k}). \tag{A5}$$

APPENDIX B: APPROXIMATION FOR OPERATOR

To approximate the nonlocal operator $\hat{O}_{(x,y)}$ by a partial differential operator of the type (6) we consider at first the homogeneous case, described by Eq. (A5). We take into account that for small values of $|\mathbf{k}|$ the operator with Fourier image (A5) can be approximated by the polynomial

$$\hat{O}_{(x,y)} = -\sum_{i,j=0}^{N} a_{ij} k_x^i k_y^j \tag{B1}$$

with a_{ij} being the coefficients of a Taylor series expansion of Eq. (A5). The value of N in Eq. (B1), must be large enough to correctly approximate Eq. (A5). Due to the invariance of the whole problem against reflections in (x,y) plane, the operator $O(\mathbf{k})$ must be an even function of both k_x and k_y and the coefficients a_{ij} are complex quantities, in general, satisfying therefore the condition $a_{ij} = 0$ for odd i or j. Taking into account that two tilted waves with nonzero value of $\mathbf{k}$ must have a minimal threshold [the maximal value of $\mathrm{Re}O(\mathbf{k})$] in accordance with the solution of the linear problem for the infinite case [10,11,25,26]), the smallest proper value of N in Eq. (B1) is equal to 4.

It is worth to note that in generally the curves $L(\mathbf{k})$ and $G(\mathbf{k})$ can be obtained only numerically. Hence, the coefficients a_{ij} need to be evaluated by a fitting procedure of the numerically obtained curve $O(\mathbf{k})$. For our case, the best precision is given by an approximation of real and imaginary parts of Eq. (B1) separately by different methods.

Since the tilted wave selection mechanism described by the approximated operator should select the same harmonics at threshold as the exact one, fitting of real part is based on the global and local extremal points of $\mathrm{Re}O(\mathbf{k})$ [see Fig. 5(a)]. We choose for that the zero point $(0,0)$, two points at every axes $(\pm k_{x0}, 0)$ and $(0, \pm k_{y0})$ and four points at the bisectrices $(\pm k_{bi}, \pm k_{bi})$. In the isotropic case all the points lay on a cycle with $|k_{x0}| = |k_{y0}| = \sqrt{2}|k_{bi}|$ with the same value of

$\mathrm{Re}O$ at these points. Denoting $o_{r0} \equiv \mathrm{Re}O(0,0)$, $o_{rx} \equiv \mathrm{Re}O(k_{x0}, 0)$, $o_{ry} \equiv \mathrm{Re}O(0, k_{y0})$, and $o_{bi} \equiv \mathrm{Re}O(k_{bi}, k_{bi})$ we have

$$a_{40}^{(r)} = (o_{r0} - o_{rx})/(k_{x0}^4),$$

$$a_{04}^{(r)} = (o_{r0} - o_{ry})/(k_{y0}^4),$$

$$a_{22}^{(r)} = (\alpha_0 o_{r0} + \alpha_x o_{rx} + \alpha_y o_{ry} + \alpha_{bi} o_{bi})/(k_{xy0}^4 k_{x0}^4 k_{y0}^4),$$

$$a_{20}^{(r)} = -2(o_{r0} - o_{rx})/(k_{x0}^2),$$

$$a_{02}^{(r)} = -2(o_{r0} - o_{ry})/(k_{y0}^2),$$

$$a_{00}^{(r)} = o_{r0},$$

where $a_{ij}^{(r)} = \mathrm{Re}\, a_{ij}$, and $\alpha_0 = -k_{bi}^4 k_{x0}^4 + 2k_{bi}^2 k_{x0}^4 k_{y0}^2 - k_{bi}^2 k_{y0}^4 + 2k_{bi}^2 k_{x0}^2 k_{y0}^4 - k_{x0}^4 k_{y0}^4$, $\alpha_x = k_{bi}^4 k_{y0}^4 - 2k_{bi}^2 k_{x0}^2 k_{y0}^4$, $\alpha_y = k_{bi}^4 k_{x0}^4 - 2k_{bi}^2 k_{y0}^4 k_{x0}^2$, $\alpha_{bi} = k_{x0}^4 k_{y0}^4$.

For an approximation of the imaginary part of $O(\mathbf{k})$, a standard least square fitting method was used (A5). The error between the exact function (A5) and the approximation (B1) for $|\mathbf{k}| \leqslant 1$ is less than 1%. It is also should be noted that changing the coefficient a_{00} leads to shift of λ_g for all g as a whole. Since we are interested here only in the order of eigenfunction it can be chosen arbitrarily. We chose a_{00} in such a way, that $O(0,0) = 0$. In the anisotropic case (10) $a_{40} = a_{04} = a_{22}/2 \equiv b_1$ and $a_{20} = a_{02} \equiv b_2$.

For convenience, we give here the numerical values of coefficients a_{ij} for the cavity described in the Sec. II, and the following parameters of underlying system: $\kappa = 2.9 \times 10^{11} s^{-1}$, $\alpha = 3$, $\delta = 10$ $nm, 6.5$ nm. For the former value of the detuning they are $a_{00} = 0$, $a_{20} = 1.165 - 0.606i$, $a_{02} = 1.166 - 0.599i$, $a_{22} = -1.42 - 0.0568i$, $a_{40} = -0.67 - 0.0071i$, $a_{04} = -0.72 - 0.0387i$ and for the latter one: $a_{00} = 0$, $a_{20} = 1.0397 - 0.606i$, $a_{02} = 1.005 - 0.56i$, $a_{22} = -2.04 - 0.057i$, $a_{40} = -0.991 - 0.0072i$, $a_{04} = -1.0369 - 0.0387i$. It is noticeable that the anisotropy of coefficients is quite small.

To write the approximation of operator $\hat{O}$ in the case, when μ and n_i are functions of (x,y), we note that $\hat{L}$ can be written in the form $\hat{L} = \hat{L}_{hom} + iln_i$, where $\hat{L}_{hom}$ describes the device with the homogeneous refractive index. In addition, we suppose that the pump profile $\mu(x,y) = \mu_0 + \delta\mu(x,y)$ consists of a constant term μ_0 and a small spatially dependent term $\delta\mu$. Then, one can expand the operator $\hat{G}$ into series such as the operator $\hat{O}$ in Eq. (B1) (but with coefficients g_{ij}), and neglect all the derivatives of $\delta\mu$ in Eq. (A4). As a result, the Eq. (A4) takes the following form:

$$\hat{O}_{(x,y)}e = -\hat{L}_{hom}e + \mu\hat{G}e + (iln_i + g_{00}\delta\mu)e. \tag{B2}$$

It is clear from above that $g_{00} = \kappa(1 + i\alpha)$. Denoting $-\hat{L}_{hom} + \mu\hat{G}$ as $\hat{O}_{hom}$, we obtain

$$\hat{O}_{(x,y)} = \hat{O}_{hom} + (iln_i + g_{00}\delta\mu). \qquad (\text{B3})$$

Taking into account that the expression for the homogeneous part of the operator $\hat{O}_{hom}$ has been already obtained by Eq. (6), and incorporating the homogeneous part of pumping μ_0 into the coefficient a_{00} in Eq. (6) for simplicity, we get the inhomogeneous approximation (11). However, it should be noted again that (11) is valid only for only small inhomogeneity $\delta\mu$, such that its spatial derivatives can be neglected compared to μ_0. Besides, n_i is also to be small enough to make the effective index approximation valid. The last restriction, however, is not so strong as the first one [47].

APPENDIX C: THE METHOD OF NUMERICAL SOLUTION OF EIGENPROBLEM (2)

1. Decomposition of fourth order eigenproblem into a generalized eigenproblem of the second order.

Our method of solution of the problem (2) is based on the fact that the operator $\hat{O}_{hom}$ can be represented via multiplication of two operators $\hat{P}_1, \hat{P}_2$ of the second order with constant coefficients

$$\hat{O}_{hom} = \hat{P}_1\hat{P}_2 e - l_1 = \hat{P}_2\hat{P}_1 e - l_1 \qquad (\text{C1})$$

where $P_1 = \nabla \cdot (\mathbf{c}_{12} \otimes \nabla), P_2 = \nabla \cdot (\mathbf{c}_{21} \otimes \nabla)$. Here $\mathbf{c}_{ij}$ are matrices defined later in (C7) and (C8), ∇ is an operator of gradient in space (x,y), $(\cdot)$ represents a scalar product and $\otimes$ means a convolution product by outer dimensions: $(a \otimes b)_{jk} = \Sigma_{i=1}^2 a_{ij}b_{ki}$. The second equality in Eq. (C1) means that $\hat{P}_1$ and $\hat{P}_2$ are commutative. By introducing an auxiliary function

$$e_1 = \hat{P}_2 e, \qquad (\text{C2})$$

or

$$e_1 = \hat{P}_1 e, \qquad (\text{C3})$$

one can present the initial eigenproblem as a generalized eigenproblem of the type

$$\hat{\mathbf{P}}\mathbf{e} - \lambda_g \mathbf{d}\mathbf{e} = 0 \qquad (\text{C4})$$

for vector function $\mathbf{e} = (e, e_1)$. Matrix $\mathbf{d}$ is a degenerate matrix $\mathbf{d} = \text{diag}(1, 0)$ (here and later $\text{diag}(\cdot, \cdot)$ means a diagonal matrix with corresponding elements on the diagonal), and the operator $\hat{\mathbf{P}}$ is defined as following:

$$\hat{\mathbf{P}} = \nabla \cdot (\mathbf{c} \otimes \nabla) + \mathbf{a}. \qquad (\text{C5})$$

Here $\mathbf{a}$ is a 2×2 matrix, $\mathbf{c}$ is a rank four tensor which can be described by four 2×2 matrices $\mathbf{c}_{ij}$. $\mathbf{a}$ and $\mathbf{c}$ for the case (C2) are determined by the following formulas:

$$\mathbf{c}_{11} = 0, \quad \mathbf{c}_{22} = \mathbf{0}, \qquad (\text{C6})$$

$$\mathbf{c}_{12} = \text{diag}[(a_{22} + l_0)/2, a_{04}], \qquad (\text{C7})$$

$$\mathbf{c}_{21} = \text{diag}[(a_{22} - l_0)/(2a_{04}), 1], \qquad (\text{C8})$$

$$\mathbf{a} = \begin{pmatrix} a_{00} - l_1 + in_i + \mu & l_2 - l_3 \\ l_2 + l_3 & -1 \end{pmatrix}, \qquad (\text{C9})$$

where l_i are given by expressions

$$l_0 = \sqrt{a_{22}^2 - 4a_{40}a_{04}}, \qquad (\text{C10})$$

$$l_1 = (a_{04}a_{20}^2 - a_{22}a_{20}a_{02} + a_{40}a_{02}^2)/l_0^2, \qquad (\text{C11})$$

$$l_2 = (2a_{04}a_{20} - a_{22}a_{02})/(2l_0), \qquad (\text{C12})$$

$$l_3 = a_{02}/2. \qquad (\text{C13})$$

The problem in the form (C4) and (C5), is suitable for solution by the finite difference method (see second part of this Appendix).

The above mentioned decomposition is not unique. The operator $\hat{P}_1$ can be multiplied by any constant, whereas $\hat{P}_2$ needs to be divided by the same constant. In addition the matrices $\mathbf{c}_{12}$ and $\mathbf{c}_{21}$ can be changed to

$$\mathbf{c}_{12} = \text{diag}[(a_{22} - l_0)/2, a_{04}], \qquad (\text{C14})$$

$$\mathbf{c}_{21} = \text{diag}[(a_{22} + l_0)/(2a_{04}), 1], \qquad (\text{C15})$$

which corresponds to a selection of e_1 according (C3). For the numerical procedure it is most natural to solve the system with simple boundary conditions (see second part of this Appendix). It is known from general theory [41] that for the system (C4) two boundary conditions satisfying a so-called Lopatinsky (or ellipticity) condition are required. We consider here the conditions $\mathbf{e} = 0$ on the boundary. For the initial eigenproblem (2) this condition on e_1 implies a condition of the type (8) with t defined as $(a_{22} \pm l_0)/(2a_{04})$ with minus for Eq. (C2) and plus for Eq. (C3). Because in the former case $|t| \leq 1$, whereas in the latter one $|t| \geq 1$, these cases can be considered as bounding of the isotropic boundary condition with $t = 1$ from bottom and from above. As Fig. 10, shows, these two cases are very close to each other for both large and small diameter of the aperture. Therefore, both of them can be considered as very good approximation of the case $t = 1$. We note again, that this result is valid if the anisotropy of operator $\hat{O}_{hom}$ is small as in the present case.

2. Numerical solving procedure

The operator $\hat{\mathbf{P}}$ in the form (C5) is suitable for solving the eigenproblem numerically, both for homogeneous (6) and inhomogeneous (11) case, by a finite element method [54]. A set of appropriate test two-component vector-functions ϕ_i is selected, and the system (C4) is presented as a set of integral equations

$$\int_\Omega \langle \phi_i, (\hat{\mathbf{P}} - \lambda_g \mathbf{d})\mathbf{e}\rangle dxdy = 0, \qquad (\text{C16})$$

where $\langle \mathbf{e}, \phi_i \rangle$ is a scalar product in two dimensional space, and Ω is the circle with radius R. Representation (C5) allows to integrate Eq. (C16) by parts, giving linear finite eigenproblem for a vector $\{p_i\}$:
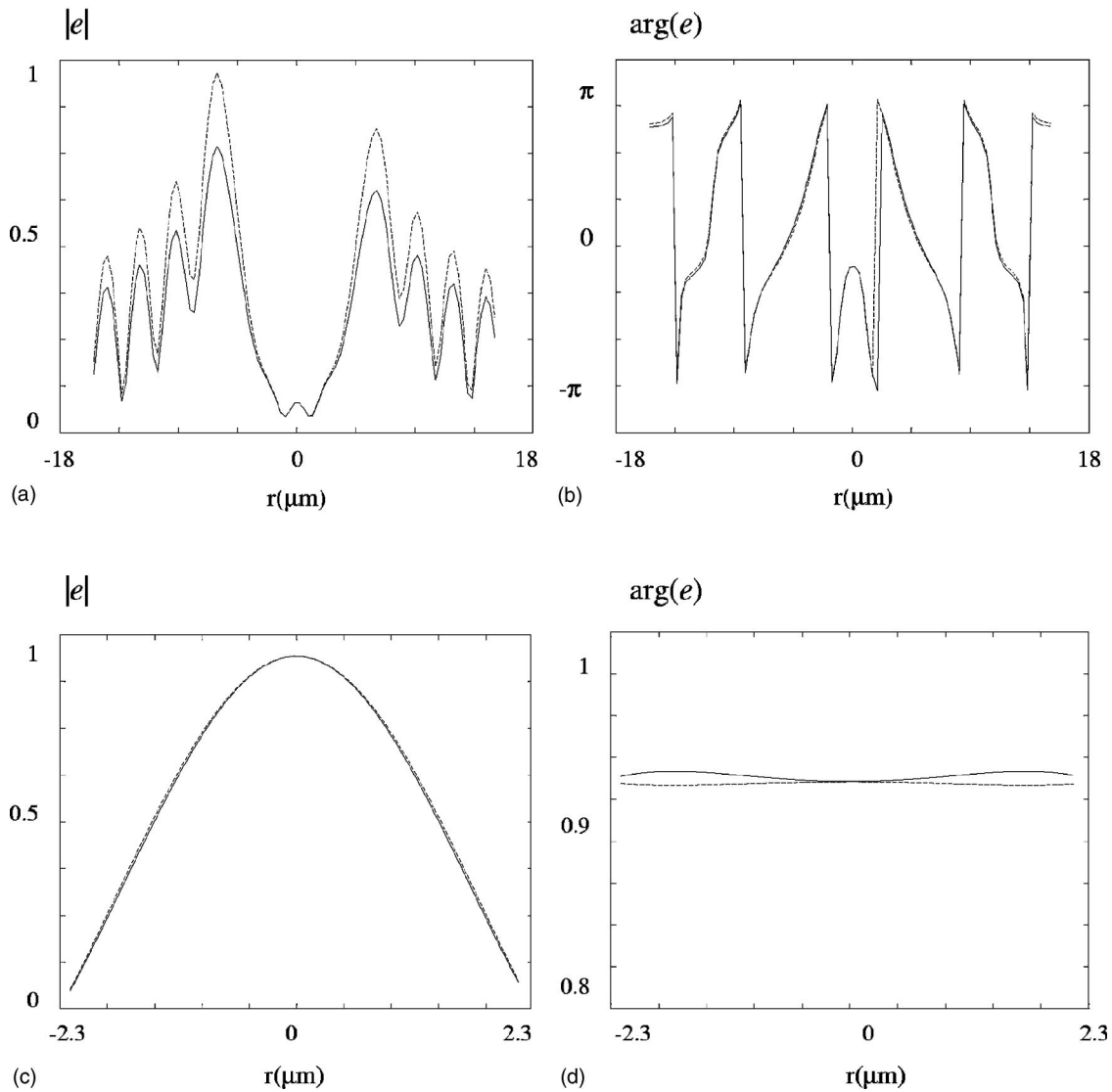
FIG. 10. The cross section of eigenmodes for different second boundary conditions. (a),(b) Stripelike modes for diameter $2R=36$ μm. (c),(d) Almost rotationally symmetric modes for smaller diameter $2R=4.6$ μm. (a),(c) are the absolute values, (b),(d) the arguments. The corresponding eigenvalues are exactly the same in all cases. Solid line is for the second boundary condition (8) defined from the decomposition (C2) whereas dashed one is for the decomposition (C3).

$$\sum_j p_j \int_\Omega \langle \nabla \phi_j, (\mathbf{c} \otimes \nabla)\phi_i \rangle + \langle \phi_j, \mathbf{a}\phi_i \rangle dx dy$$

$$- \lambda_g \sum_j p_j \int_\Omega \langle \phi_j, \mathbf{d}\phi_i \rangle dx dy = 0, \qquad (C17)$$

where zero boundary conditions (7) and (8) are taken into account, and $\{p_i\}$ represent approximate decomposition of $\mathbf{e}$ in a finite basis ϕ_i: $\mathbf{e} = \Sigma_j p_j \phi_j$. The system (C17) was solved numerically by Arnoldi method [55], using Matlab PDE Toolbox.

[1] C. J. Chang-Hasnain, M. Orenstein, A. V. Lehmen, L. T. Florez, J. P. Harbison, and N. G. Stoffel, Appl. Phys. Lett. **57**, 218 (1990).

[2] H. Li, T. L. Lucas, J. G. McInerney, and R. A. Morgan, Chaos, Solitons Fractals **4**, 1619 (1994).

[3] I. Hörsch, R. Kusche, O. Marti, B. Weigl, and K. J. Ebeling, J.

Appl. Phys. **79**, 3831 (1996).

[4] M. Grabherr, R. Jäger, M. Miller, C. Thalmaier, J. Herlein, and K. J. Ebeling, IEEE Photonics Technol. Lett. **10**, 1061 (1998).

[5] S. Hegarty, G. Huyet, J. G. McInerney, and K. D. Choquette, Phys. Rev. Lett. **82**, 1434 (1999).

[6] J. Scheuer and M. Orenstein, Science **285**, 230 (1999).

[7] T. Ackemann, S. Barland, M. Cara, S. Balle, J. R. Tredicce, R. Jäger, P. M. Grabherr, M. Miller, and K. J. Ebeling, J. Opt. B: Quantum Semiclassical Opt. **2**, 406 (2000).

[8] C. Degen, I. Fischer, W. Elsäßer, L. Fratta, P. Debernardi, G. Bava, M. Brunner, R. Hövel, M. Moser, and K. Gulden, Phys. Rev. A **63**, 023817 (2001).

[9] K. F. Huang, Y. F. Chen, H. C. Lai, and Y. P. Lan, Phys. Rev. Lett. **89**, 224102 (2002).

[10] N. A. Loiko and I. V. Babushkin, Quantum Electron. **31**, 221 (2001).

[11] N. A. Loiko and I. V. Babushkin, J. Opt. B: Quantum Semiclassical Opt. **3**, S234 (2001).

[12] M. Grabherr, M. Miller, R. Jäger, R. Michalzik, U. Martin, H. J. Unold, and K. J. Ebeling, IEEE J. Sel. Top. Quantum Electron. **5**, 495 (1999).

[13] M. Miller, M. Grabherr, R. King, R. Jäger, R. Michalzik, and K. J. Ebeling, IEEE J. Sel. Top. Quantum Electron. **7**, 210 (2001).

[14] S. Hegarty, G. Huyet, P. Porta, J. G. McInerney, K. D. Choquette, K. M. Geib, and H. Q. Hou, J. Opt. Soc. Am. B **16**, 2060 (1999).

[15] P. K. Jakobsen, J. V. Moloney, A. C. Newell, and R. Indik, Phys. Rev. A **45**, 8129 (1992).

[16] J. Lega, J. Moloney, and A. Newell, Phys. Rev. Lett. **73**, 2978 (1994).

[17] K. Staliunas and C. O. Weiss, Physica D **81**, 79 (1995).

[18] Y. F. Chen, K. F. Huang, and Y. P. Lan, Phys. Rev. E **66**, 046215 (2002).

[19] Y. F. Chen, K. F. Huang, H. C. Lai, and Y. P. Lan, Phys. Rev. Lett. **90**, 053904 (2003).

[20] D. Burak and R. Binder, IEEE J. Quantum Electron. **33**, 1205 (1997).

[21] G. Liu, J.-F. Seurin, S. L. Chuang, D. I. Babic, S. W. Corzine, M. Tan, D. C. Barnes, and T. N. Tiouririne, Appl. Phys. Lett. **73** 726 (1998).

[22] G. P. Bava, P. Debernardi, and L. Fratta, Phys. Rev. A **63**, 023816 (2001).

[23] J. Mulet and S. Balle, IEEE J. Quantum Electron. **38**, 291 (2002).

[24] N. A. Loiko, A. V. Naumenko, and N. B. Abraham, Laser Phys. **10**, 861 (2000).

[25] N. A. Loiko and I. V. Babushkin, Proc. SPIE **4751**, 382 (2002).

[26] I. V. Babushkin, N. A. Loiko, and T. Ackemann, Phys. Rev. A **67**, 013813 (2003).

[27] J. Lega, J. Moloney, and A. Newell, Physica D **83**, 478 (1995).

[28] M. Bestehorn and R. Friedrich, Phys. Rev. E **59**, 2642 (1999).

[29] R. Michalzik, M. Grabherr, and K. J. Ebeling, Proc. SPIE **3286**, 206 (1998).

[30] J. Martín-Regalado, F. Prati, M. S. Miguel, and N. B. Abraham, IEEE J. Quantum Electron. **33**, 765 (1997).

[31] M. Travagnin, M. P. V. Exter, A. K. Jansen, A. K. J. V. Doorn,

and J. P. Woerdman, Phys. Rev. A **54**, 1647 (1996).

[32] M. Sondermann, M. Weinkath, T. Ackemann, J. Mulet, and S. Balle, Phys. Rev. A **68**, 033822 (2003).

[33] L. A. Coldren and S. W. Corzine, *Diode Lasers and Photonic Integrated Circuits* (Wiley, New York, 1995).

[34] F. T. Arecchi, S. Boccaletti, and P. L.Ramazza, Phys. Rep. **318**, 1 (1999).

[35] T. Rössler, R. A. Indik, J. V. Moloney, D. Burak, R. Binder, and T. Ackemann (unpublished).

[36] A. E. Siegman, *Lasers* (University Science Books, Mill Valley, California, 1986).

[37] E.-G. Neumann, *Springer Series in Optical Sciences* (Springer, Berlin, 1988), Vol. 57.

[38] T. E. Sale, *Vertical Cavity Surface Emitting Lasers* (Wiley, New York, 1995).

[39] M. Grabherr, B. Weigl, G. Reiner, R. Michalzik, M. Miller, and K. J. Ebeling, Electron. Lett. **32**, 1723 (1996).

[40] A. Barchansky, C. Degen, I. Fisher, and W. Elsässer, IEEE J. Quantum Electron. **39**, 850 (2003).

[41] L. Hörmander, *The Analysis of Linear Partial Differential Operators* (Springer, Berlin, 1985).

[42] L. A.Lugiato, W. Kaige, L. M. Narducci, G. L. Oppo, M. A. Pernigo, J. R. Tredicce, D. K. Bandy, and F. Prati, J. Opt. Soc. Am. B **5**, 879 (1988).

[43] J. W. Miller, *Symmetry and Separation of Variables* (Cambridge University Press, Cambridge, 1977).

[44] P. Jakobsen, J. Lega, Q. Feng, M. Staley, J. Moloney, and A. Newell, Phys. Rev. A **49**, 4189 (1994).

[45] A. D. Polianin, *Handbook of Linear Partial Differential Equations for Engineers and Scientists* (CRC Press, Boca Raton, 2001).

[46] K. J. Ebeling, in *Semiconductor Quantum Optoelectronics: From Quantum Physics to Smart Devices*, edited by A. Miller, M. Ebrahimzadeh, and D. M. Finlayson (SUSSP Publications, Bristol, 1999), pp. 295–338.

[47] G. R. Hadley, Opt. Lett. **20**, 1483 (1995).

[48] I. V. Babushkin (unpublished).

[49] O. G. Calderón, E. Cabrera, M. Antón, and J. M. Guerra, Phys. Rev. A **67**, 043812 (2003).

[50] M. C. Bowden and J. P. Dowling, Phys. Rev. A **47**, 1247 (1993).

[51] M. Le Berre, E. Ressayre, and A. Tallet, Phys. Rev. E **67**, 066207 (2003).

[52] C. H. Henry, IEEE J. Quantum Electron. **18**, 259 (1982).

[53] W. H. Press, B. Flannery, S. Teukolsky, and W. Vettering, *Numerical Recipes: The Art of Scientific Computing* (Cambridge University Press, Cambridge, 1992).

[54] R. D. Cook, D. S. Malkus, and M. E. Plesha, *Concepts and Applications of Finite Element Analysis* 3rd ed. (Wiley, New York, 1989).

[55] Y. Saad, Linear Algebr. Appl. **35**, 269 (1980).

[56] M. Born and E. Wolf, *Principles of Optics* (Pergamon, New York, 1980).